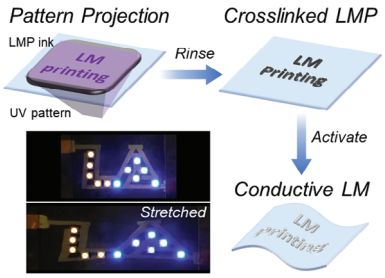

A digital light processing-based liquid metal printing strategy using a photo-crosslinkable ink is described. This technique patterns stretchable eutectic gallium-indium with high resolution (≈20 µm), excellent conductivity (3×10^6 S m^{-1}), extreme stretchability (≈2500%), and excellent stability under various deformations. Its potential is showcased in applications like stretchable circuits, wearable electronics, and soft robotics.

ADVANCED MATERIALS
www.advmat.de

Fast and Facile Liquid Metal Printing via Projection Lithography for Highly Stretchable Electronic Circuits

*Dong Wu, Shuwang Wu, Poom Narongdej, Sidi Duan, Chi Chen, Yichen Yan, Zixiao Liu, Wen Hong, Imri Frenkel, and Ximin He**

Soft electronic circuits are crucial for wearable electronics, biomedical technologies, and soft robotics, requiring soft conductive materials with high conductivity, high strain limit, and stable electrical performance under deformation. Liquid metals (LMs) have become attractive candidates with high conductivity and fluidic compliance, while effective manufacturing methods are demanded. Digital light processing (DLP)-based projection lithography is a high-resolution and high-throughput printing technique for primarily polymers and some metals. If LMs can be printed with DLP as well, the entire soft devices can be fabricated by one printer in a streamlined and highly efficient process. Herein, fast and facile DLP-based LM printing is achieved. Simply with 5–10 s of patterned ultraviolet (UV)-light exposure, a highly conductive and stretchable pattern can be printed using a photo-crosslinkable LM particle ink. The printed eutectic gallium indium traces feature high resolution (≈20 µm), conductivity (3×10^6 S m^{-1}), stretchability (≈2500%), and excellent stability (consistent performance at different deformation). Various patterns are printed in diverse material systems for broad applications including stretchable displays, epidermal strain sensors, heaters, humidity sensors, conformal electrodes for electrography, and multi-layer actuators. The facile and scalable process, excellent performance, and diverse applications ensure its broad impact on soft electronic manufacturing.

1. Introduction

Circuits, complete circular paths made of conductive materials enabling electricity to flow through, are the most basic elements required for all electronics. Soft circuits have drawn tremendous interest in a broad range of emerging technologies such as wearable electronics,[1,2] biomedical devices,[3] human–machine interface,[4] and soft robotics.[5] Besides high conductivity and reliable signal transmission, many new characteristics are demanded over traditional rigid electronics such as light weight, flexibility, stretchability, and conformability. Extensive research has been undertaken to develop new material systems and fabrication techniques, yet challenges remain in various aspects of soft electronic manufacturing and performance.[6]

In recent decades, stretchable circuits have been created by fabricating inextensible conductive materials into unique flexible structures, such as serpentine ribbons and out-of-plane arc-shaped structures, to gain deformability and stretchability.[7–9] Despite the maturity and compatibility of the fabrication techniques with conventional rigid electronic components, structure-based stretchable circuits could only provide limited stretchability. Conductive composites with conductive fillers, such as carbon materials,[10,11] metallic micro/nanomaterials[12–14] in elastomer matrices, and interlocked metal nanoparticle-elastomer bilayer structures,[15,16] offer an alternative solution. Although the stretchability was improved, most composites sacrifice conductivity due to the limited conductive paths in the polymeric matrix and poor interface between conductive fillers. Therefore, conductors with intrinsic stretchability have attracted great interest including ionic conductors,[17] conducting polymers,[18] and room-temperature liquid metals (LMs).[19] Among these novel materials, gallium-based LMs, especially eutectic gallium indium (EGaIn), provide much higher electrical conductivity and larger stretchability, attributed to their unique metallic and fluidic nature at room temperature. Additionally, EGaIn has been studied extensively due to its unique properties such as water-like viscosity, low toxicity, high thermal conductivity, neglectable volatility, and the formation of oxide skin.[19,20] It is also widely used in wearable electronics,[21–25] epidermal sensing,[26–28] thermal devices,[29–33] and soft robotics.[34–37]

LM has been fabricated into various two-dimensional/three-dimensional (2D/3D) soft circuits with diverse fabrication techniques.[38-40] Conventional manufacturing methods, such as stencil printing,[41] laser ablation,[42] and photolithography,[43-45] have been used. Taking advantage of its fluid nature, LM can be injected or vacuum-filled into soft microfluidics and porous templates.[46,47] Selectively wetting of LM on rigid metal patterns was also reported.[48,49] In addition, additive manufactur-

D. Wu, S. Wu, P. Narongdej, S. Duan, C. Chen, Y. Yan, Z. Liu, W. Hong, I. Frenkel, X. He
Department of Materials Science and Engineering
University of California
Los Angeles (UCLA), Los Angeles, CA 90095, USA
E-mail: ximinhe@ucla.edu

The ORCID identification number(s) for the author(s) of this article can be found under https://doi.org/10.1002/adma.202307632

DOI: 10.1002/adma.202307632

ing strategies have been utilized to print LM including inkjet printing,[50] direct writing,[51,52] thermal transfer printing,[53] adhesive assisted printing,[54] and magnetic/voltage/freezing assisted printing.[20,55] Digital light processing (DLP) as one of the most popular additive manufacturing technologies, which generates high-quality light patterns by modulating light via a micromirror array, has been used to fabricate 2D patterns/3D objects of polymer, ceramic, and metal materials.[56-63] Despite the excellent accuracy and resolution, as well as relatively high printing efficiency (owing to its parallel process vs. other serial ones), DLP has not yet been reportedly used for printing conductive LM circuits.

Even though bulk LM has been used for fabricating soft circuits, its high surface tension largely hinders its applications, due to the issues of limited resolution, discontinuous fluid during jetting, and unreliable connection under strain. Therefore, the increasing amount of research suggests using liquid metal particles (LMPs) instead, which can be easily obtained by applying shear or vibration to bulk LM. The oxide skin of LMP not only diminishes the tension ensuring the relative ease of manipulation, but also endows LMP with unique surface reactivity, which substantially extends its applications.[64] To fabricate soft circuits, LMPs were usually cast or molded with a polymer matrix into films and foams, then sintered with laser or localized pressure to form conductive paths, which led to limited inter-particle connection, low resolution, and low material utilization rate (only a small fraction of LMP regions being activated).[65,66] Recently, advanced strategies using LMP composites to fabricate stretchable circuits with excellent electromechanical properties have been reported. Liu et al. invented a biphasic EGaIn via oxidation and phase segregation at high temperatures.[67] Neumann et al. developed a self-encapsulating LMP-Polydimethylsiloxane composite for direct write printing.[68] Lee et al. reported an ultrasonication strategy, which can promote the connection between LMPs in various polymer matrices.[69] Despite satisfactory performance, the high-energy-input and multi-step fabrication process, the possible nozzle clogging issue due to the build-up oxidation and polymer solidification, or reliance on a physical mask for patterning, persuade further searching for a novel and energy-saving fabrication solution with high efficiency and moderate processing conditions.

Herein, we introduce a facile and scalable strategy to rapidly (5–10 s) fabricate highly conductive (3×10^6 S cm^{-1}) LM patterns with extreme stretchability (>2500%) at high resolution (≈20 µm), via DLP-based projection lithography for the first time. Such highly conductive and stretchable LM patterns are printed by projecting ultraviolet (UV) patterns onto a photo-reactive ink containing chemically-functionalized LMPs and polymer precursors. The modified LMPs were covalently crosslinked with a confining polymeric layer via photopolymerization, followed by mechanical sintering (gentle rubbing or peeling with tapes to break oxide barriers between LMPs) to further promote electrical conductance. Uniquely, the in situ photo-polymerization and photo-crosslinking allowed for the formation of an LM-polymer bilayer structure (rather than mixed as in composites), where an adhesive polymer thin layer formed beneath (rather than inside) the LM layer anchors and confines the LMPs tightly on the stretchable substrate and precisely within the illuminated area via covalent and hydrogen bonding. Thus, the resulting continuous LM layer as an electron-conduction highway, strongly and dynamically bound onto a stretchable adhesive polymer thin layer, enables the superior stable high conductivity upon large deformation and high resolution.

Advantageously, the entire fabrication process is conducted in ambient conditions at room temperature with a simple light exposure for a few seconds at a low energy input. The critical parameters of the pattern formation, including ink formulation and light exposure, have been systematically investigated. We have also carefully studied the electromechanical performance of the printed EGaIn, under twisting, bending, and stretching. To explore the potential of this printing method, we have demonstrated a broad range of applications for diverse on-body electronics, including an epidermal strain sensor for gesture monitoring, an electrically driven heater for thermal therapy, a humidity sensor for breath and finger contact, and conformal electrodes for electrophysiology monitoring. Additionally, the LM traces have been printed into various thin-film soft actuators including a multi-layer electromagnetic actuator and electroactive liquid crystal elastomer (LCE) actuators.

2. Result and Discussion

2.1. Fabrication and Mechanism of LM Printing

The facile procedure of printing highly conductive liquid metal patterns with the LMP ink consisted of four steps (**Figure 1**a and Video S1, Supporting Information). First, the ink was drop-cast on a transparent substrate. After seconds until the LMPs ink became still, a designed UV light pattern was projected from the bottom of the substrate at the interface between the ink and substrate, using a DLP projection system with a 385 nm UV light source. Within 5–10 s of exposure, a non-conductive crosslinked LMP (cLMP) pattern with a thickness of around 5 µm can be printed on the substrate. The non-crosslinked components were then washed away with ethanol and a clear cLMP pattern can be obtained. At last, the cLMP pattern was activated to be highly conductive with simple mechanical sintering such as pressing, rubbing, and peeling.

It is noticeable that rapid printing speed, high printing resolution, and flexible pattern design of the printed LM (Figure 1c,d) can be achieved simultaneously due to the implementation of DLP, which utilizes a digital micromirror device to generate light patterns. The intrinsic maskless parallel printing process and the rapid photo-crosslinking reaction of this method guarantees high throughput manufacturing. This is demonstrated by the rapid printing of a 3 × 3 array of a circuit pattern with a UV exposure for 10 s (Figure 1e), which significantly reduced the fabrication time, compared to other additive techniques such as direct writing (>1 min). In addition, cLMPs can be printed on rigid, flexible, and stretchable substrates. A stretchable "LM" circuit was printed on a polystyrene-block-polyisoprene-block-polystyrene (SIS) rubber substrate and connected with LEDs as a visual indicator, which remained the stable connection while being repeatedly stretched to 70% strain (Figure 1f and Video S2, Supporting Information). The as-fabricated LM pattern on SIS achieved a high conductivity of 3×10^6 S m^{-1} and well retained the conductance at a maximum strain of 2500%, which stood out of the state-of-the-art stretchable conductors (Figure 1g).

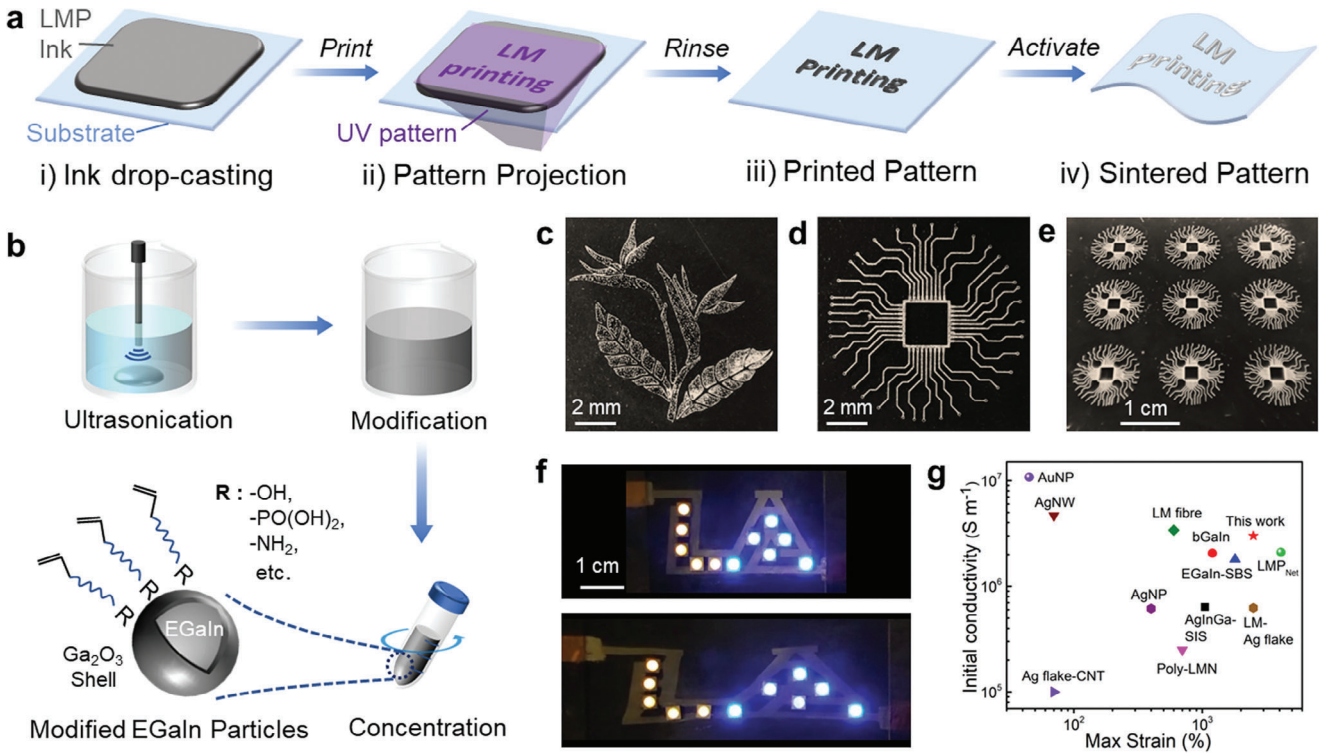

Figure 1. Fabrication of conductive liquid metal patterns via DLP-based projection lithography. a) Schematic of the printing process: i) drop-casting of LMP ink; ii) UV pattern projection on the substrate; iii) obtaining the printed cLMP pattern after rinsing off non-reacted components; iv) activation to form a conductive flexible LM pattern, via mechanical sintering such as pressing, rubbing, and peeling. b) Schematic of modified LMP stock solution preparation: bulk LM was first broken into LMPs in ethanol under ultrasonication; the dispersion was kept still for the anchoring of modifying agent to anchor to the oxide shell of LMPs afterward; the modified LMPs solution was then rinsed and concentrated by centrifuging to obtain the modified LMP stock solution. c–e) Images of printed LM patterns of a Strelitzia reginae (bird of paradise flower), a circuit, and a circuit array; f) A stretchable LM circuit printed on an SIS substrate connected with LEDs; g) Comparison of initial conductivity and stretchability with various stretchable conductors: silver flakes and multiwalled carbon nanotubes in styrene isoprene block copolymer rubber (Ag flake-CNT),[10] silver nanoparticles (AgNP),[12] silver nanowires (AgNW),[13] gold nanoparticles (AuNP),[70] silver microflakes with EGaIn in styrene isoprene block copolymer rubber (AgInGa-SIS),[71] biphasic Ga-In (bGaIn),[67] EGaIn-coated poly(styrene-block-butadiene-block-styrene) microfiber mat (EGaIn-SBS),[72] polymerized liquid metal networks (Poly-LMN),[66] liquid metal fiber (LM fiber),[73] liquid metal and silver flakes in polyurethane acrylate elastomer (LM-Ag flake),[74] and long-range assembled network of LMPs (LMP_{Net}).[69]

To achieve fast LM patterning via DLP projection lithography, it is critical to develop a unique photo-patternable LMP ink. The first step toward the printable ink is to make the LMPs photo-crosslinkable (Figure 1b). To create chemically modified LMPs (mLMPs), we mixed bulk LM with modifying agents in ethanol and shattered them via ultrasonic shearing (Figure 1b). The mLMP-ethanol dispersion was kept still in ambient condition for several hours before being centrifuged to obtain mLMPs. Then the mLMPs were rinsed and centrifuged with fresh ethanol solvent to remove the unreacted agents. Thus, a concentrated mLMP solution was obtained serving as a stock solution. The modifying agents have one end anchoring on the mLMP shell and the other end photo-crosslinkable with other mLMPs and polymers. Specifically, the mLMPs have their Ga_2O_3 shell chemically bonded with ligands via anchoring groups, which can be hydroxyl, thiol, phosphonic acid, carboxylic acid, silane, and amine.[64,66,75–77] The ligands ending with alkene or thiol groups can enable the subsequent photo-crosslinking. Thus, broad choices of compounds can function as the modifying ligands to make LMPs photo-printable, as we experimentally verified, including 2-hydroxyethyl acrylate (2-HEA), 3-(trimethoxysilyl) propyl methacrylate, allylamine, acrylamide, 1,6-hexanedithiol, acrylic acid, and 11-phosphonoundecyl acrylate (11-PUA). Different ligands could lead to slightly different morphologies, chemical compositions, and particle sizes, while all of them can serve their purpose of making LMPs photo-crosslinkable. In the following experiments and demonstration, we specifically used 2-HEA to modify LMPs. As the mLMP stock solution was prepared, we adequately mixed it with other components, including crosslinker, dispersant, monomer, and photoinitiator, at an appropriate ratio to form the photo-printable LMP ink (see details in the Experimental Section). The monomer used in this work is 2-HEA, as it can form an adhesive polymer layer that well confines mLMPs ending with 2-HEA ligands and enables high stretchability and stable conductivity, as discussed in detail as follows.

To further understand and optimize this printing technique, we first investigated the pattern formation process. Since the LMPs in the ink would precipitate due to their high density, the LMP ink was homogenized with vortex prior to printing. As the ink turned into a dark grey dispersion without obvious lamination, we drop-cast an adequate amount of ink onto the substrate. We observed that the LMPs in the dropped solution

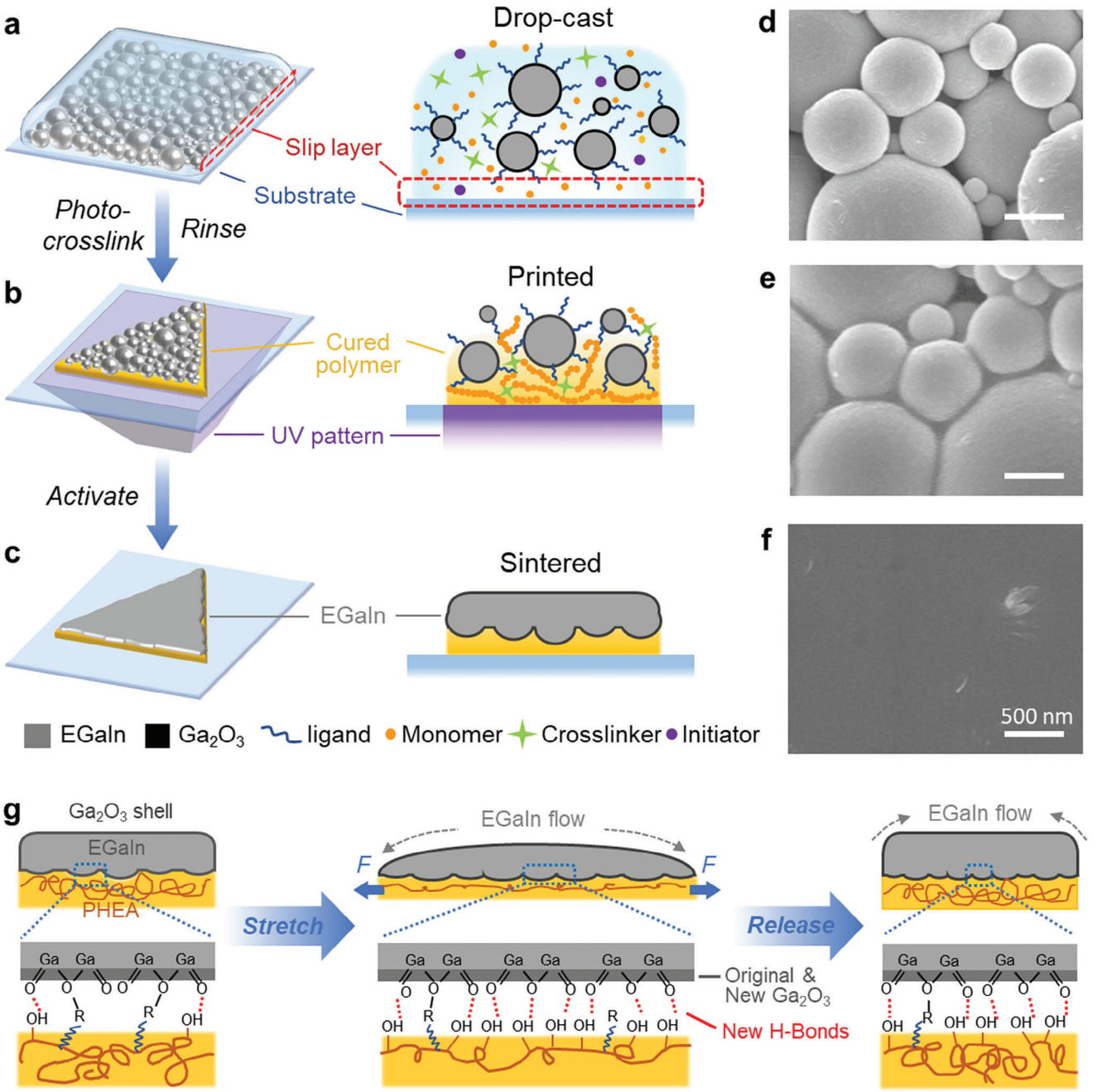

Figure 2. Mechanism of LM printing via DLP-based projection lithography. General and zoom-in schematics of a) the drop-cast LM ink on a substrate, b) the printed cLMP network, and c) the LM-PHEA bilayer structure after activation. d–f) The SEM images corresponding to stages (a), (b), and (c), respectively. g) Schematic of interfacial reconciliation between the EGaIn and the PHEA layer upon stretching and releasing via newly formed hydrogen bonding, enabling high electromechanical performance with consistently high conductivity upon stretching.

would precipitate within seconds. Although oxide skin formed as the shell of LMPs, the particles did not stick to the substrate like bulk EGaIn, which can be attributed to a slip layer of ink formed between the LMPs and the substrate (**Figure 2a**). The thin slip layer could prevent the adhesion of LMPs to the substrate, as previously suggested by Mohammad et al.[78] We further validated this observation by a tilting test, where glass substrates with the LMP ink cast onside were tilted before and after the full evaporation of ethanol solvent (Figure S1, Supporting Information). We suggested that the presence of the slip layer not only prevents the direct adhesion of LMPs ensuring the uncrosslinked LMPs to be easily rinsed off, but also facilitated the formation of an adhesive polymer layer in the following step. Once the LMPs in the cast ink precipitated, a UV-light pattern was projected from the bottom through the substrate onto the ink-substrate interface, to crosslink the mLMPs and polymerize

the monomer 2-HEA within the slip layer. Upon UV exposure, the photoinitiator, diphenyl(2,4,6-trimethylbenzoyl)phosphine oxide (TPO), absorbed the UV radiation and underwent homolytic cleavage to produce free radicals. Once the free radicals were generated, they would be added to the alkene group in different components to initiate the free radical polymerization. The initiated polymer chain is propagated by the addition of alkene groups in monomers, modified LMPs, or crosslinkers to the radical molecules.[79] Eventually, the mLMPs were chemically bonded with the polymer forming the cLMP layer. The UV intensity and duration had a significant effect on the double bond conversion yield and polymerization rate, which directly determined the printing quality.[80,81] Detailed investigations are showcased in the following Section 2.2. After light exposure and subsequent rinsing, the cLMPs pattern was obtained on the substrate. The modification of LMPs and the usage of adhesive monomer 2-HEA work synergistically to precisely confine the LMPs to the designed area and promote printing uniformity. By contrast, voids and lower precision in the printed patterns were observed when omitting the LMP modification and/or 2-HEA, as shown by our comparison experiments (Figure S2, Supporting Information). The absence of LMP modification could lead to uneven printing of patterns. Without surface ligands to crosslink the LMPs with polymer, LMPs have a higher chance to merge into larger droplets, which can deplete the surrounding small LMPs and form LM islands across the patterns, disturbing the continuity of the conductive paths (Figure S2b, Supporting Information). Together with the lack of a 2-HEA monomer additive, the LM islands could be easily removed during rinsing, leaving voids in the pattern (Figure S2a, Supporting Information). Even printed with mLMPs in ink, abundant missing spots could be observed with the omission of 2-HEA (Figure S2c, Supporting Information). Therefore, only with both the LMP modification and 2-HEA, we were able to form a uniform cLMP pattern accurately. To observe the adhesive polymer layer beneath the cLMP layer, the Ga_2O_3 shell was reduced and the cLMPs were etched away using sodium hydroxide, and a polymeric poly-2-hydroxyethyl acrylate (PHEA) layer formed beneath the cLMPs layer was revealed and confirmed (Figure S3, Supporting Information). Therefore, we concluded that the presence of the slip layer led to the formation of an adhesive PHEA layer at the bottom of the printed structure holding the cLMPs onside (Figure 2b).

To obtain the conductance, the cLMPs pattern was then subject to shearing stress for activation. The applied stress would cause the rupture of the thin oxide layer and allow the EGaIn liquid inside the LMPs to flow out and coalesce (Figure 2c). Due to the remerging nature of EGaIn, conductive paths would form throughout the desired pattern. The morphological evolution throughout the different stages of the printing process was confirmed with scanning electron microscopy (SEM) (Figure 2d–f). The mLMPs exhibited well-defined outlines after being drop-cast on the substrate (Figure 2d). After UV exposure, the LMPs were interconnected through the adhesive PHEA that filled the gaps between them (Figure 2e). Upon activation, cLMPs were broken while EGaIn liquid inside coalesced to form a continuous layer (Figure 2f). Both EGaIn layer and PHEA layer have a thickness of around 3 µm. Importantly, the PHEA layer consists of abundant hydroxyl groups, and enables a native-oxide-driven interface reconciliation of EGaIn onsite under mechanical deformation (Figure 2g), which contributed to the high stretchability of the printed conductor.[82] In detail, as the printed traces were subject to strain, the soft segments of PHEA and EGaIn both would be stretched. Stretching of PHEA would expose an increasing amount of -OH groups on the polymer chains to the EGaIn. Meanwhile, attributed to the fluidic nature of EGaIn and the existence of an inextensible Ga_2O_3 shell, the original Ga_2O_3 layer would be torn apart while a new EGaIn surface would be generated, new Ga_2O_3 layer would also form spontaneously with the presence of oxygen. The oxygen could come from both ambient air and cavities in the printed pattern. The newly generated Ga_2O_3 and the newly exposed EGaIn interface would interface with the numerous —OH on the stretched PHEA, forming hydrogen bonding to guide the EGaIn to deform with the substrate. Once the strain is released, the EGaIn with Ga_2O_3 shell would reconfigure its surface to adapt to the post-stretched PHEA layer. Overall, such a bilayer structure ensured the compliance of EGaIn with the stretchable substrate, providing superior electromechanical performance and high stability over directly mixing LMPs with a soft polymer matrix.

Despite the significant advantages, the bilayer structure limits the ability to stack multiple print layers. The adhesive polymer can act as an insulating layer preventing the electrical current flow between stacked LM layers. In addition, the bottom-up projection makes it difficult to stack layers. Therefore, the DLP-based method currently has limitations for forming freestanding 3D circuits which can be easily achieved by direct writing-based 3D printing methods.[83,84] However, we believe that it would be possible to print freestanding 3D circuits with a DLP-based 3D printing method by developing new material systems of inks to generate LM-polymer interpenetrating structures through which electrons can travel.

2.2. Critical Parameters in Printing

To understand the critical parameters that determine the quality of the printed patterns, we investigated the particle size of LMPs, the input power density of light, the crosslinker concentration, and the LMP concentration. First, the average particle sizes (**Figure 3a**) and distribution of LMPs modified with 2-HEA (Figures S4 and S5, Supporting Information) were measured. We observed that the particle sizes largely depended on the ultrasonication amplitude and time. With the increase in the ultrasonication amplitude from 20% to 40% and the time extending from 5 to 15 min, the average size of LMPs modified with 2-HEA decreased from 1.2 µm to ≈320 nm. Similar trends were also observed with LMPs modified with 11-PUA (Figures S6 and S7, Supporting Information). However, different modifying agents also have an influence on the average particle sizes (Figure S12, Supporting Information). With these different-sized mLMPs evaluated, we discovered that the particle size had a significant effect on the patterning accuracy and the required input power density. Specifically, we designed a pattern of eight strips with different line widths ranging from 22.5 µm to 1.44 mm and printed it with different LMP inks, which consisted of LMPs prepared with 20% amplitude and 5-, 10-, and 15-min sonication time, respectively. As we exposed the inks to a UV pattern of 2.58 mW cm^{-2}, only seven strips were printed and the thinnest

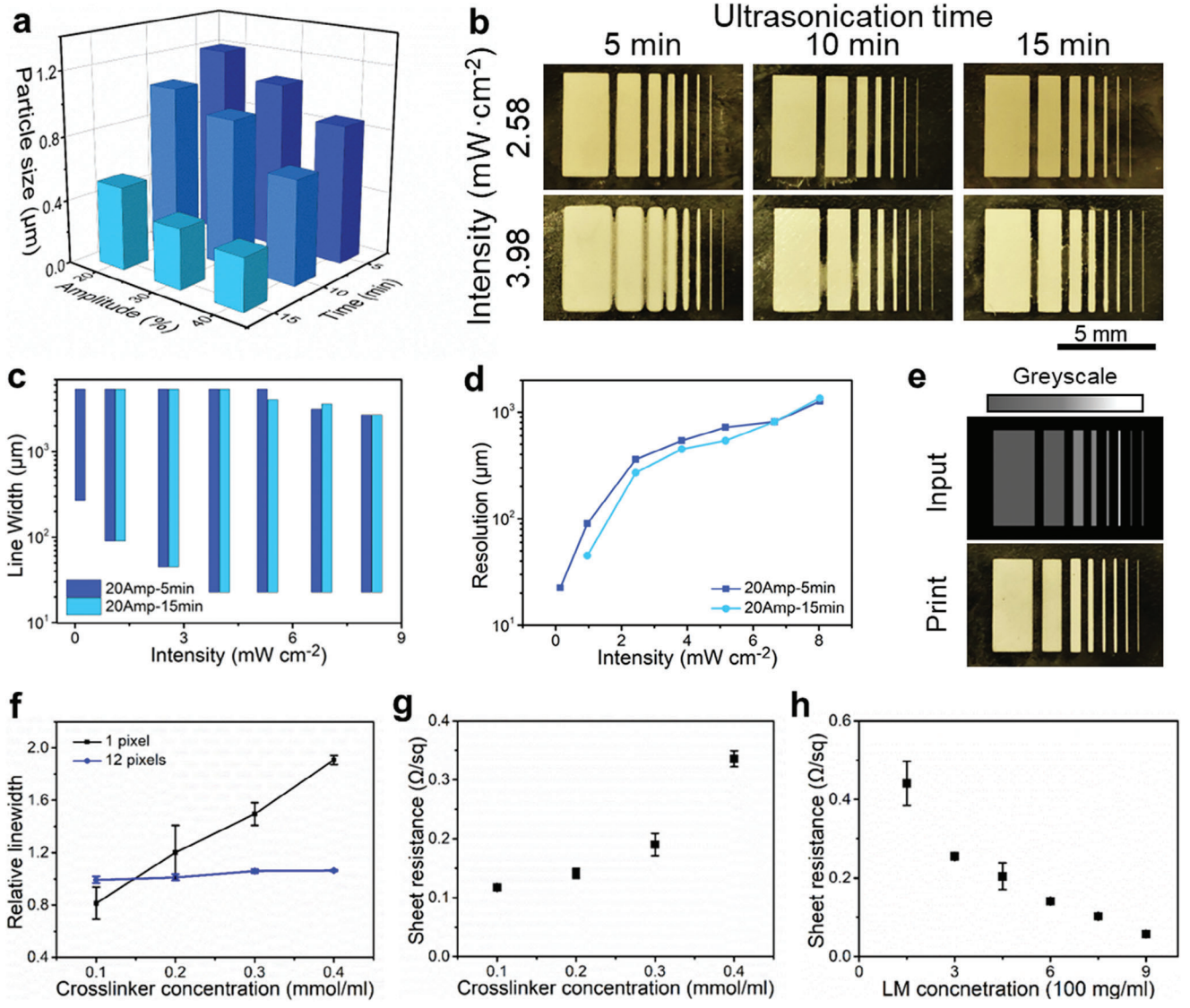

Figure 3. Investigation on critical parameters in the fabrication process. a) Average LMP sizes under different ultrasonication amplitude (20% to 40%) and time (5 to 15 min). b) Images of the strip patterns printed with different light intensities using LMP inks prepared by different ultrasonication conditions. c) Linewidth range of the printed strips with varied input power density. d) Resolution of the printed traces with varied input power density. e) A greyscale digital image (top) and corresponding printed LMP pattern (bottom). f) Relative linewidths of printed strips using inks with varied crosslinker concentrations. g) Sheet resistance of printed pattern as a function of crosslinker concentration in LMP inks. h) Sheet resistance of printed pattern as a function of LM concentration in LMP inks.

one was always absent for each print. By increasing the power input to 3.98 mW cm^{-2}, all eight strips could be printed, which indicated that higher light intensity was required to achieve the printing with thinner features. However, it is notable that increasing intensity can lead to the inaccurate printing of larger features. Blurred edges and filled gaps between strips were observed on the samples printed with higher input power (Figure 3b). In addition, we observed that smaller particle sizes can help create clear outlines of the printed features under exposure to the same light intensity. We also observed that both the illumination intensity and the particle size have great effects on the height (or thickness) and the relative linewidth of the printed patterns (Figures S21–S23, Supporting Information). The increasing intensity could lead to increased height and width, which could be attributed to the enhancement of light penetration depth and light scattering in the ink. The reduction in particle size in a certain range by increasing ultrasonication time might decrease both the height and width of the printed features. However, an opposite relation was also observed while both height and width increased as the particles got smaller. Future studies may be conducted to better understand the influence of various parameters.

To obtain an overall picture of the relation between average particle sizes and the input power density, we designed patterns of strips and gaps with the line width ranging from 22.5 μm to 5.4 mm using two LMPs inks (20% amplitude, 5 min, and 15 min, noted as 20Amp-5min and 20Amp-15min). Then we

printed the patterns with UV light of varied input power density, ranging from 0.14 to 8.03 mW cm^{-2}, and measured the achievable linewidth of strips (Figure 3c), as well as the resolution (Figure 3d). With an exposure intensity of 0.14 mW cm^{-2}, no pattern can be printed with the 20Amp-15min ink, while the thinnest linewidth can be obtained with the 20Amp-5min ink was 270 µm. By increasing the light intensity, thinner lines became achievable for both inks. As the input power density increased to 3.83 mW cm^{-2}, the thinnest linewidth (22.5 µm) this printing setup can provide was achieved, with the 20Amp-5min ink upon illumination of 10 s. A further rise in input power will lead to the falling part of the printed larger patterns during rinsing, which can be attributed to the uneven photopolymerization and the failure of a continuous PHEA layer formation due to the overly high input power. Therefore, we expected that there would be an optimized range of input power for printing with different LMP inks. Moreover, resolution was another significant characteristic of printing, which was defined as the width of the smallest gap that could be printed. The increase in input power density would boost the feature size that can be resolved. The decrease in particle sizes could help achieve higher resolution with proper input power. The combination of linewidth and resolution studies would give guidance on the design of patterns and the control of power input. Herein we demonstrated an example by printing the same 8-strip pattern at different greyscales (Figure 3e). With proper greyscale distribution, we printed the pattern with one exposure, which was clearer and more accurate compared to those printed with simple black-and-white images (Figure 3b).

In addition to particle size and input power density, we also investigated the influence of crosslinkers and LMP concentrations on the printing results. Various crosslinkers can serve for this material system, while trimethylolpropane ethoxylate triacrylate was used in this study. The 20Amp-5min LMP inks with the same LMP concentrations of 450 mg mL^{-1} and different crosslinker concentrations ranging from 0.1 to 0.4 mmol mL^{-1} were prepared to study the printed linewidth and sheet resistance. The relative linewidth is defined as the ratio of the printed linewidth to the designed linewidth. Relative linewidths of strips printed from digital images of 1- and 12-pixel designed widths using different crosslinker concentrations were measured. For the 1-pixel strip which was designed to be 22.5 µm, the actual printed linewidth increased along with the increasing crosslinker concentration, while the relative linewidth had negligible change for the 12-pixel strip (Figure 3f). However, both strips had a comparable variation at a width of around 20 µm with the increase of crosslinker concentration. Therefore, we suggested that the crosslinker concentration has a tremendous effect on the polymerization of LMPs at the edges of the printed patterns. The higher the concentration was, the more LMPs would be crosslinked at pattern outlines. In addition, the increase in crosslinker concentration would also lead to the formation of a more resilient PHEA-LMP network, making it more difficult to break the oxide shell of the LMPs during the sintering. The tougher crosslinked network limited the formation of conductive paths, which eventually raised the sheet resistance of the printed patterns (Figure 3g). To decrease the sheet resistance of the conductive traces, the most simple and effective way is to increase the LM concentration in the LMP ink. By raising the LM concentration from 150 to 900 mg mL^{-1}, a rapid decrease in the sheet resistance from 0.441 to 0.057 Ω/square can be observed (Figure 3h). However, simply increasing the LM concentration would lower the printing resolution (Figure S28, Supporting Information). For LM inks with various LM concentrations, different printing parameters, such as intensity, would be required in order to achieve the desired resolution. With the optimized ink composition and printing parameters, we were able to print various patterns with desirable performance.

2.3. Electromechanical Performance

To evaluate the electromechanical performance of the LM patterns fabricated in this work, we printed and activated EGaIn traces on a flexible substrate and stretchable substrate and measured their relative resistance change (R/R_0) undergoing twisting, bending, and uniaxial stretching (**Figure 4a**). The traces printed on SIS had an outstanding stable electromechanical performance with inconspicuous resistance change under various twisting angles up to 360° (Figure 4b). For traces on flexible but non-stretchable substrates like PET, electromechanical performance is commonly evaluated by bending tests. By bending the traces printed on PET thin film inward and outward respectively at a radius ranging from 2 to 24 mm, negligible resistance change ($\Delta R/R_0 \approx \pm 0.01$) was observed (Figure 4c). Furthermore, we conducted 10 000 cycles of outward bending with a radius of 1 mm on the printed trace where limited resistance change ($\Delta R/R_0 < 0.03$, $\Delta R < 0.05$ Ω) was observed (Figure 4d).

To unveil the stretching limitation of the LM traces, we printed the pattern on highly stretchable SIS thin film and measured the change in resistance as a strain was put on the samples (Figure 4e). The printed trace showed satisfactorily low resistance change at low strain and notably high stretchability. The resistance changes measured at low strain ($R/R_0 \approx 1.22$ at 100% strain and $R/R_0 \approx 3.74$ at 500% strain) are much smaller than the theoretical prediction for an incompressible, constant-conductivity bulk liquid metal conductor using Pouillet's law ($R/R_0 = (1+\epsilon)^2$, where ϵ is the applied strain; $R/R_0 = 4$ at strain of 100%, $R/R_0 = 36$ at strain of 500%). As the strain further increased from 500% to 2200%, the resistance increased linearly with the strain. Once the strain exceeded the critical point at 2200%, the resistance ascended rapidly until the substrate failed. We observed that at such a high strain, the PHEA layer on the substrate was not fully covered by the LM layer due to the enlargement of the surface area during stretching and the insufficient amount of LM to maintain the coverage. Despite this, the tested sample can remain conductive at such high strain (>2500%). In addition, we studied the cyclic stretching performance of the printed trace by subjecting it to a cyclic strain of 100% (Figure 4f). At the initial cycles, the resistance went through an adapting stage with some increase and then settled to a stable electromechanical platform over 1500 cycles. The resistance increase is believed to be attributed to the interfacial mismatch between the solid copper tape electrodes and liquid EGaIn. In accordance with the study of the electrotechnical performance of the printed samples, the conductive traces possessed excellent stretchability and stability under strain. Yet, the challenges in optimizing the interface between printed circuits and external connection, especially mounted electronics components, are expected to be addressed in the future.

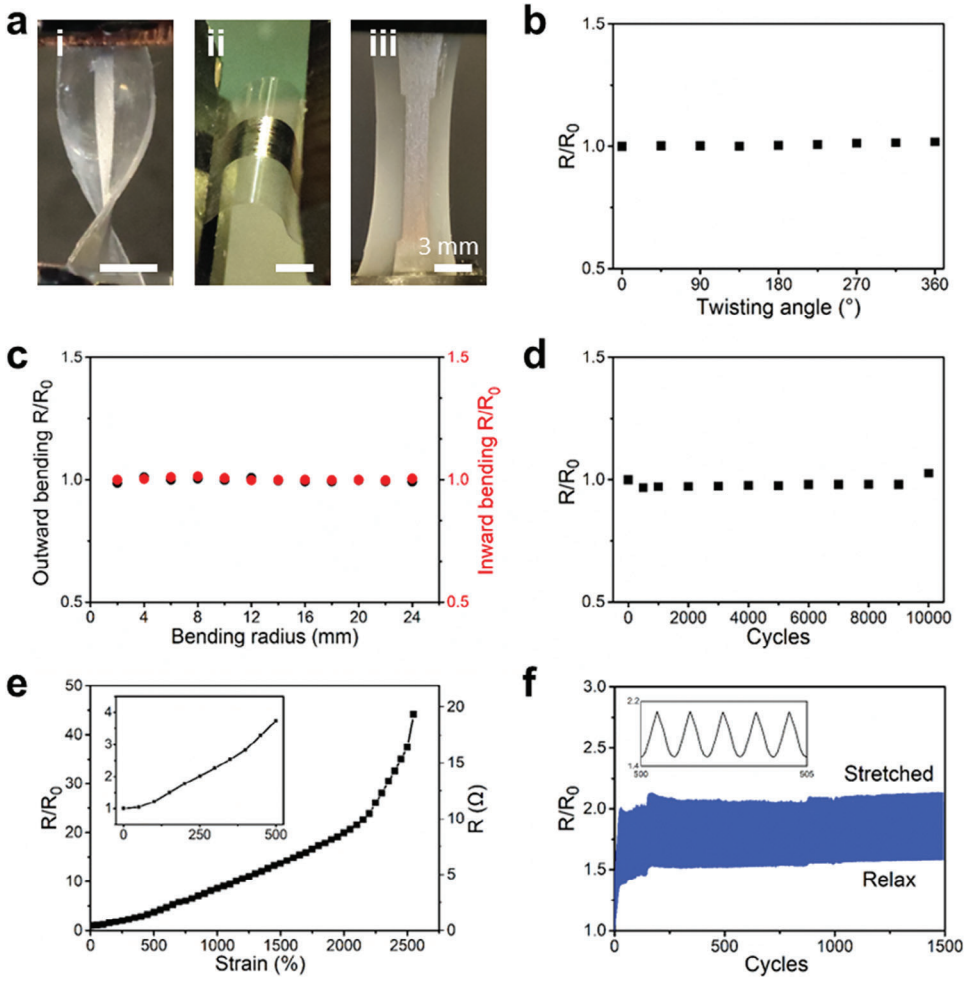

Figure 4. Electromechanical characteristics of printed LM patterns. a) Printed LM traces subjected to i) twisting, ii) bending, and iii) stretching. b) Relative resistance changes as a function of twisting angle. c) Relative variation in resistance under outward (black) and inward (red) bending with a bending radius from 2 to 24 mm; d) Relative resistance change of printed LM trace subjected to cyclic bending with a radius of 1 mm up to 10 000 cycles. e) Relative resistance/resistance (Ω) variation as a function of strain. f) Relative variation in resistance during cyclic stretching at a strain of 100% up to 1500 cycles.

2.4. Printed LM for Flexible Devices

To demonstrate the patterning capability of our printing method and the excellent electrical and electromechanical performance of the printed EGaIn, we fabricated several flexible/stretchable wearable devices, including an electrically driven heater for thermal therapy, a humidity sensor for breath monitoring, conformal electrodes for electrophysiology monitoring, a strain sensor for soft haptics, and a capacitive sensor for detecting finger contact (**Figure 5**). First, we printed a wave-shaped LM pattern serving as a resistive heater. The IR image (Figure 5a) showed the temperature distribution of the heater in an ambient environment and after being powered with 5 V for 1 min. The average temperature of the substrate can rise to around 80 °C within a minute (Video S3, Supporting Information). We also investigated the relation between the applied voltage and the temperature of the heater. By applying different voltages from 1 to 5 V, we were able to control the heating temperature from 28 to 83 °C (Figure 5b). Besides, we printed LM on SIS to fabricate an epidermal ohmic strain sensor to detect finger motions. The sensor was attached conformably to the index finger of the tested human subject. As the finger switched between the relaxed state and bending states of angles of 45° and 90°, the resistance of the conductive pattern varied accordingly based on the bending angle (Figure 5e and Video S4, Supporting Information). The stable cycling performance and instant response to deformation allowed the strain sensor to serve as an effective interface for tracking human body motions (Figure 5f and Video S5, Supporting Information).

In addition to Ohmic devices, we were able to fabricate a capacitive sensor via integrating a printed interdigitated LM pattern and a cast polyvinyl alcohol (PVA) thin film onside (Figure 5c inset graph). PVA as a hygroscopic polymer can be utilized in fast and stable humidity sensing due to its abundant hydroxyl groups.[85–87] With the excellent compatibility between the LM circuit and PVA coating, this thin-film sensor can be easily fabricated to detect humidity change and provide electrical output, which can serve as a breath sensor. With the sensor placed 2 cm in front of the volunteer's nose, the tested subject breathed in

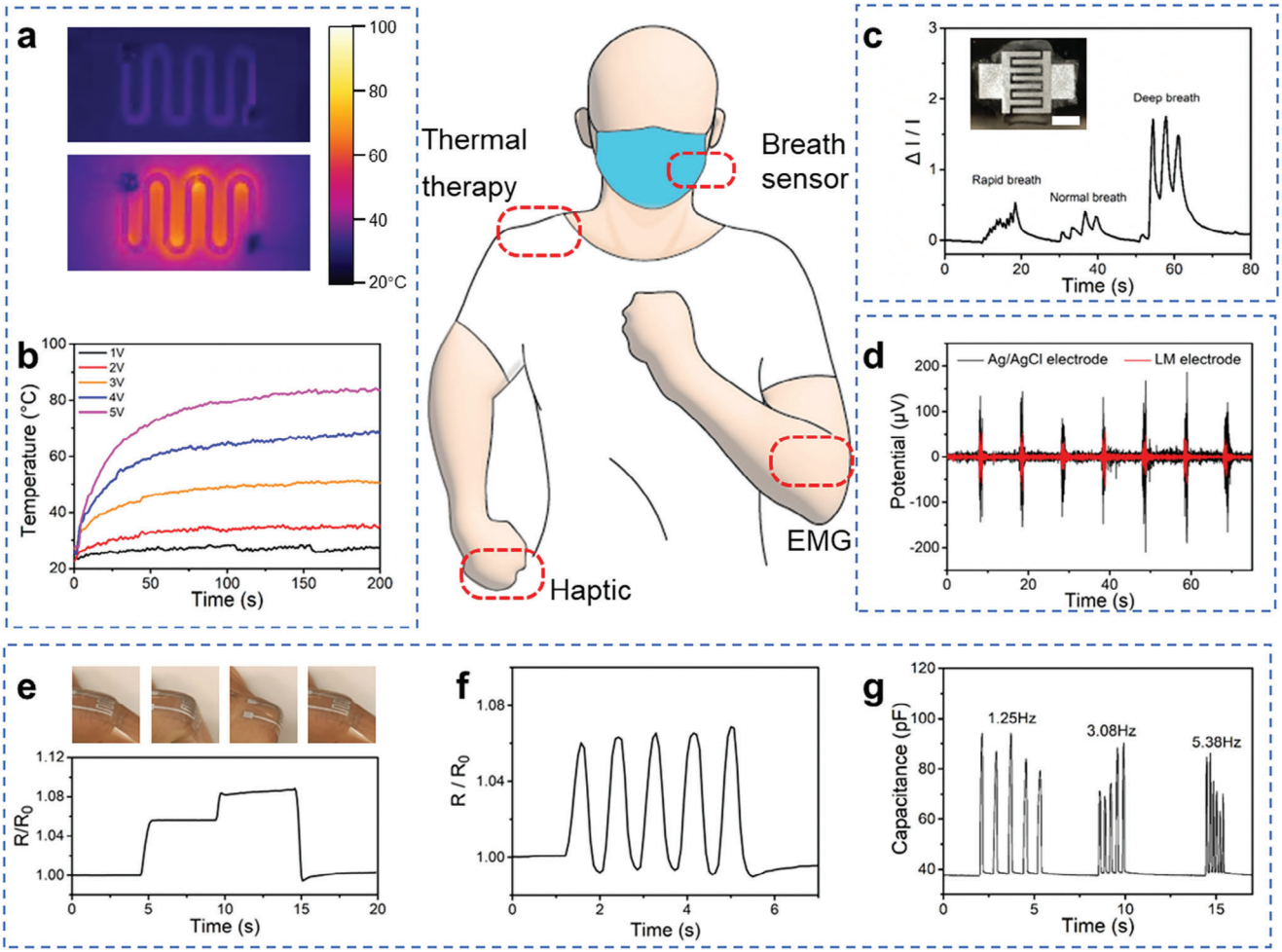

Figure 5. Applications of printed LM circuits for wearable electronics. a) IR thermal images of the LM heater with wave structure for thermal therapy before and after applying a 5 V voltage input. b) Temperature evolution of the flexible LM heater with constant applied voltages from 1 to 5 V. c) Leakage current curve of the proposed breath sensor for sensing different breath patterns. d) Electromyography (EMG) signals collected by LM electrodes (red) and commercial Ag/AgCl electrodes (black). e) Resistance variation of the LM strain sensor on a finger bending with different angles. f) Resistance variation of the LM strain sensor under multiple finger-bending cycles. g) Capacitance curve of the proposed sensor for the finger contact at different frequencies of 1.25, 3.08, and 5.38 Hz.

diverse ways including unevenly rapid breathing, normal breathing, and deep breathing. Each exhalation led to an increase in the humidity of the PVA sensing layer. By measuring the leakage current of the capacitive sensor under 0.5 V voltage, different breathing modes can be obviously identified (Figure 5c). Such a breath sensor has the potential to achieve complex breath monitoring by anchoring other electrochemical sensing materials to the printed circuit. Additionally, the same configuration can be utilized to detect finger proximity/contact, as moisture retained by dry fingers can cause a sudden change in capacitance. We recorded the capacitance variation of the sensor under the tapping of a dry finger of the volunteer at varied frequencies (Figure 5g). With different finger flapping frequencies from 1.25 to 5.38 Hz, the sensor could identify each contact between the finger and the PVA layer.

Furthermore, we fabricated a conformal stretchable electrode patch for electromyography (EMG) signal monitoring (Figure 5d). A three-electrode LM pattern was printed on an SIS substrate and activated to achieve conductivity. A SIS thin film with a hole pattern was laminated above to seal the conductive trace, leaving the contact electrodes exposed. The patch was then conformably attached to the human subject's forearm epidermis (Figure S14, Supporting Information). The EMG signals were recorded by the LM patch clearly and continuously, comparable to those collected by the commercial Ag/AgCl electrodes. The safe and reliable acquisition of EMG signals suggested broader potential applications with our LM printing technique in electrophysiological studies and diagnosis.

Apart from wearable devices, our printing method holds the potential for fabricating circuits and electrodes intended for invasive medical devices. We demonstrated such potential through the application of printed stretchable electrodes on a balloon catheter designed for angioplasty or stent placement (Figure S15, Supporting Information). A set of LM electrodes with extended conductive traces was printed on SIS and affixed to the catheter's balloon. These printed traces appeared to possess a fine 20 μm linewidth. As the balloon was inflated and deflated, the electrodes

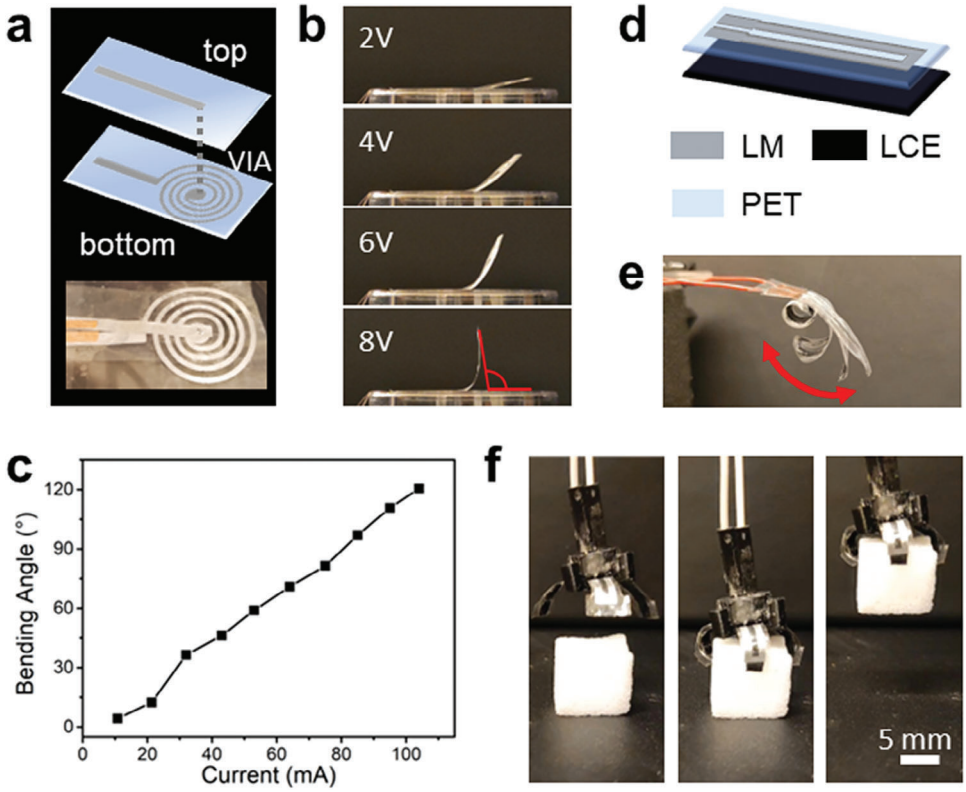

Figure 6. Applications of printed LM circuits for soft robotics. a) Schematic and image of the bilayer thin film electromagnetic actuator. b) Images of the actuator bending with varied input voltages. c) Bending angle variation as a function of applied current. d) Schematic of the bilayer LM-LCE actuator. e) Images of the bilayer LM-LCE actuator rolling up with an input current of 100 mA. f) LM-LCE gripper picking up a soft sponge cube via electrothermal actuation.

stretched and relaxed conformably to the balloon, ensuring uninterrupted performance (Figure S15c,d and Video S9, Supporting Information).

The outstanding electromechanical properties and the simple fabrication process of the printed LM drove us to exploit its applications in the field of soft robotics. Therefore, we fabricated two types of flexible thin-film actuators based on different mechanisms. A multilayer thin-film electromagnetic actuator was demonstrated first (**Figure 6**a–c). A spiral and a rectangular conductive pattern were first printed on PET substrates separately (Figure 6a). A vertical interconnect access (VIA) was created on the top layer by laser cutting. Then the two layers were laminated and a small drop of LM was injected into the VIA for connecting LM traces on both layers. The bilayer actuator was then fixed at one end onto a flat platform above a magnet. An input current was applied through the bilayer circuit to generate an instant magnetic field in an opposite direction to the permanent magnet. According to Ampere's Law ($\int B \cdot dI = \mu_0 I$, where B is the magnetic field, dI is an infinite element of the conductive pattern, μ_0 is the permeability of free space, and I is the current flowing through the pattern), the generated magnetic field is proportional to the applied current. Therefore, we tuned the voltage from 1 to 10 V to study the bending angle of the actuator (Figure 6b,c). The actuation was instantly controlled (Video S6, Supporting Information), and a large bending angle of around 120 degrees was achieved at a current of 100 mA.

In addition, we combined printed LM circuits with LCE to fabricate an electro-driven flexible thin-film actuator. LCE as a popular smart material with reversible shape transformation, suitable modulus, large actuation strain, and good reliability.[88,89] It consists of mesogens that can transit from a nematic state to an isotropic state with environmental stimuli such as temperature, humidity, and electric. Here we used an LCE composite which was synthesized and fabricated into thin films using our previously reported method.[90,91] The LCE thin film was then laminated with a PET thin film with LM traces printed onside to assemble the thin-film actuator (Figure 6d). By applying a current of 100 mA to the LM trace, we were able to achieve a reversible rolling-up motion of the actuator (Figure 6e and Video S7, Supporting Information). The deformation of the soft actuator can also be easily tuned by changing the input current. For an illustration of its practical application, we further integrated and demonstrated an LM-LCE gripper. A current of 80 mA was applied to actuate the gripper, picking up soft objects including a soft sponge cube (Figure 6f) and a 3D-printed hydrogel lattice (Video S8, Supporting Information). The release of the object was also achieved by simply turning off the power input, allowing the LCE to relax. These implementation results highlight the exceptional lightweight and flexibility of the soft robotics based on flexible LM circuits printed with the technique presented in this study. Besides, the compatibility of handling soft materials and the ease of integration make our LM

printing a promising solution for soft robotics and biomedical applications.

3. Conclusion

In summary, we have achieved DLP-based printing of LMs. It expands the family of photo-printable materials, primarily polymers, and regular metals in the past, with this important class of soft conductors. Compared to other LM fabrication methods through molding and serial writing process, this rapid photo-patterning technique takes advantage of the high-resolution and high throughput of DLP-based projection lithography. Thus, this facile and scalable fabrication method can pattern highly stretchable EGaIn with excellent electrical and electromechanical performance, at ambient conditions rapidly over less than a minute. The printed EGaIn features high resolution (≈20 µm), high conductivity (3×10^6 S m^{-1}), extreme stretchability over 2500%, and great cyclic stability under various types of deformation. The fundamental mechanism study and systematic fabrication process investigation help establish a design principle of ink formulation and printing process and can also guide future technique optimization and extension. To exploit this printing technique, we demonstrated a variety of soft electronic and wearable devices fabricated by this approach including epidermal sensors and electrodes, an electrically driven heater, and humidity sensors. Additionally, we showcased two types of thin-film soft actuators featuring lightweight and outstanding flexibility, including an electromagnetic actuator which can achieve large bending angles, and LM-LCE actuators which can achieve rolling-up motion. We also demonstrated an LM-LCE gripper for picking up soft objects. With the high-throughput scalable fabrication process and remarkable performance of the printed LM, we expect the presented LM printing strategy can enable low-cost mass production of flexible electronics for a wide range of applications in wearable electronics, medical devices, and soft robotics.

4. Experimental Section

Materials: Gallium (Ga) purchased from Gallant Metals and Indium (In) purchased from Luciteria Science were combined in a ratio of 75% Ga and 25% In by weight to produce EGaIn. 2-HEA, TPO, 3-(trimethoxysilyl) propyl methacrylate, allylamine, acrylamide, 1,6-hexanedithiol, acrylic acid, 11-PUA, poly(ethylene glycol) diacrylate (PEGDA), trimethylolpropane ethoxylate triacrylate (ETPTA, Mn 428 and 912), pentaerythritol tetraacrylate, trimethylolpropane triacrylate, polyethylene glycol 200 (PEO-200), 2-hydroxy-4′-(2-hydroxyethoxy)-2-methylpropiophenone (Irgacure 2959), pentaerythritol tetrakis(3-mercaptopropionate) (PETMP), 2,2′-(ethylenedioxy)diethanethiol, dipropylamine (DPA), polystyrene-block-polyisoprene-block-polystyrene (SIS), and dipolyethylene terephthalate (PET) thin films were purchased from Sigma-Aldrich, Inc. 2-Methyl-1,4-phenylene bis(4-(3-(acryloyloxy)propoxy)benzoate) (RM 257) was purchased from Shijiazhuang Sdyano Fine Chemical, Co., Ltd.. Toluene was purchased from Avantor Performance Materials. Glass slides and ethanol were purchased from Fisher Scientifics, Inc.

Material Fabrication: In all cases, 500 mg of EGaIn liquid metal was transferred via a syringe into a 20 mL vial. 20 mg surface modifying agent (2-HEA as an example agent in this work) was dissolved in 10 mL ethanol and then the solution was added to the vial. The vial was immersed approximately half of the solution level into a chilled water bath with ice, before the ultrasonication process to create EGaIn particles, specifically using a Q500 Sonicator (Qsonica Inc.). The ultrasonication procedure was set to an amplitude of 20%, 30%, and 40% and a sonication time of 5, 10, 15, and 20 min, respectively. After the ultrasonication, the clear colorless solution turned into a dark grey colloidal solution that contained EGaIn particles. The suspension was placed still in the dark overnight, allowing the modifying agents to fully react with the gallium oxide shell. Then, the solution was centrifuged in 2000 relative centrifugal force (rcf) for 3 min and the supernatant was removed and replaced. This process was repeated three times with a final suspension of EGaIn particles and 1 mL ethanol.

Precursors Formula: Different stock solutions were prepared including 150–900 mg mL^{-1} LMPs ethanol solution, 200 mg mL^{-1} PEO-200 in ethanol as the dispersant solution, and 0.1–0.3 mmol mL^{-1} ETPTA-912 in ethanol as the crosslinker solution. The printable inks in this work were prepared by mixing the above as-prepared solutions of LMPs, PEO-200, and ETPTA-912, with the adhesive monomer 2-HEA, at a volume ratio of 15:5:5:1. Finally, 0.4 vol% of TPO as photoinitiator was added into the above mixture and mixed under vortex to form the LMP inks for printing.

Printing Architecture and Procedure: The bottom-up setup consisted of a DLP-based projector PRO4500 from Wintech Digital System Technology Corporation, a motorized translation stage mounted to a motor controller, and optical accessories from Thorlabs, Inc.

The printing process was conducted under ambient conditions. Transparent substrates were placed on the translation stage and the focus of the projected patterns was adjusted to the top surface of the substrates. The LMP ink was vortexed before usage. An adequate amount of LMP ink (≈520 mL m^{-2}) was then cast on the substrates. Then a designed pattern was projected for 5–10 s and rinsed with ethanol and water to wash away the extra LMPs and solution. A designed LMPs-polymer pattern was formed and mechanical sintering, such as pressing, rubbing, and peeling, was then proceeded to make the printed traces conductive. For pressing, a PET thin film was first placed on the printed patterns and a metal rod was used to roll onside to apply compressive and shear forces on the patterns. For rubbing, a small soft sponge was used to gently rub the surface of the patterns. For peeling, adhesive tape was first applied to the patterns and then gently peeled off to achieve conductance.

Material Characterization: SEM images were taken by a ZEISS Supra 40VP SEM. The as-printed samples were observed under SEM after sputtering a thin gold layer using Pelco SC-7 sputter due to the existence of the oxide shell of LMPs. The sintered samples were directly observed without further treatment. The obtained SEM was analyzed using the software ImageJ. The particle sizes were determined by measuring the diameters of the particles. X-ray photoelectron spectra (XPS) were obtained using an X-ray photoelectron spectrometer (Axis Ultra, Kratos). The height/thickness and width of printed patterns were measured by the Veeco Dektak 8 Profilometer from Bruker Corporation.

Electrical Characterization: A rectangular pattern of LMPs with a 3:1 aspect ratio was printed on a PET substrate and activated via mechanical sintering. The sheet resistance of the printed samples was measured with a four-point probe from Suzhou Jingge Electronic Co., Ltd. and 2450 digital multimers Keithley Instrument. The thickness of the activated LM patterns was measured with Phase-Shift Interference (PSI) mode by Bruker NT9300 optical profiler from Bruker Corporation. The conductivity of activated LM patterns was calculated as the product of sheet resistance and thickness.

Electromechanical Characterization: A rectangular pattern of LMPs was printed and activated via mechanical sintering. The patterns printed on PET were for the bending test and those printed on SIS were for the stretching test. The printed samples on PET and SIS were subjected to bending and stretching, respectively, using a Unistretch mechanical tester from Cellscale Inc. The resistance of the printed LM patterns was measured using 2450 digital multimers from Keithley Instrument.

Soft Electronic Devices and Demonstrations: All LM patterns in this work were printed by using the LMP ink via DLP projection lithography as described in the printing procedure section. For the stretchable "LA" LED array, 11 LEDs were adhered to the SIS substrate. With voltage held constant at 2.7V, the LED array was put under a strain of 70% by hand and then released repeatedly. For the strain sensor, a folded trace was printed on SIS and attached to the index finger of the tested volunteer. The resistance variation was measured and recorded with 2450 digital multimers from Keithley Instrument. For the electrically driven heater, a curve trace

was printed on SIS and different voltages were applied. The temperature and IR images were measured and recorded with a TiX580 thermal imager from Fluke Corporation. For the breath sensor, a cross-finger electrode pair was printed on PET and a PVA aqueous solution was cast on the cross-finger area. The device was then placed at ambient allowing water evaporation to form a PVA humidity-sensitive film. By applying a 0.5 V voltage, the leakage current was measured and recorded using the 2450 digital multimers from Keithley Instrument. The same laminated structure can be utilized as a finger touch/proximity sensor. The capacitance change was measured and recorded using a DAQ6510 multimer system from Keithley Instrument. For the electrodes of EMG monitoring, a three-electrode pattern was printed on SIS. Then the other SIS thin film with punched holes was laminated above to seal the conductive trace. Ten 20 conductive paste was applied on the skin first and then the patch was conformably attached to the human subject's forearm epidermis. The signals were measured and recorded using a Cyton + Daisy biosensing board (16 channels) from OpenBCI Inc. For the bilayer electromagnetic actuator, a spiral and a rectangular pattern were printed on PET substrates separately. A VIA was created on the top layer by the Genmitsu PROVerXL 4030 laser cutter from SainSmart. Then the two layers were laminated and a drop of bulk LM was injected into the VIA forming a conductive path through both layers. The LCE thin film was fabricated via a reported method and then laminated with an LM circuit printed on PET. For both actuators, a silicone adhesive was used for interlayer binding, and an E36313A programmable DC power supply from Keysight Instrument was used to control the power input.

Experimental Consent: All subjects in wearable device experiments gave their informed consent prior to participation, in accordance with the ethical principles outlined in the WMA Declaration of Helsinki.

Supporting Information

Supporting Information is available from the Wiley Online Library or from the author.

Acknowledgements

The authors acknowledge the support of the start-up funds from the University of California, Los Angeles.

Conflict of Interest

The authors declare no conflict of interest.

Data Availability Statement

The data that support the findings of this study are available from the corresponding author upon reasonable request.

Keywords

eutectic gallium indium, liquid metal, projection lithography, soft electronics, stretchable circuit

Received: July 31, 2023
Revised: December 19, 2023
Published online:

[1] P. Won, S. Jeong, C. Majidi, S. H. Ko, *iScience* **2021**, *24*, 102698.
[2] M D. Dickey, *Adv. Mater.* **2017**, *29*, 1606425.
[3] B. Llerena Zambrano, A F. Renz, T. Ruff, S. Lienemann, K. Tybrandt, J. Vörös, J. Lee, *Adv. Healthcare Mater.* **2021**, *10*, 2001397.
[4] Z. Rao, F. Ershad, A. Almasri, L. Gonzalez, X. Wu, C. Yu, *Adv. Mater. Technol.* **2020**, *5*, 2000233.
[5] S I. Rich, R J. Wood, C. Majidi, *Nat. Electron.* **2018**, *1*, 102.
[6] D. F. Fernandes, C. Majidi, M. Tavakoli, *J. Mater. Chem. C* **2019**, *7*, 14035.
[7] Z. Huang, Y. Hao, Y. Li, H. Hu, C. Wang, A. Nomoto, T. Pan, Y. Gu, Y. Chen, T. Zhang, W. Li, Y. Lei, N. Kim, C. Wang, L. Zhang, J W. Ward, A. Maralani, X. Li, M F. Durstock, A. Pisano, Y. Lin, S. Xu, *Nat. Electron.* **2018**, *1*, 473.
[8] J A. Rogers, T. Someya, Y. Huang, *Science* **2010**, *327*, 1603.
[9] D.-H. Kim, N. Lu, R. Ma, Y.-S. Kim, R.-H. Kim, S. Wang, J. Wu, S. M. Won, H. Tao, A. Islam, K. J. Yu, T.-I. Kim, R. Chowdhury, M. Ying, L. Xu, M. Li, H.-J. Chung, H. Keum, M. Mccormick, P. Liu, Y.-W. Zhang, F. G. Omenetto, Y. Huang, T. Coleman, J. A. Rogers, *Science* **2011**, *333*, 833.
[10] H. S. Lee, Y. Jo, J. H. Joo, K. Woo, Z. Zhong, S. Jung, Su Y Lee, Y. Choi, S. Jeong, *ACS Appl. Mater. Interfaces* **2019**, *11*, 12622.
[11] K. Fu, Y. Yao, J. Dai, L. Hu, *Adv. Mater.* **2017**, *29*, 1603486.
[12] N. Matsuhisa, D. Inoue, P. Zalar, H. Jin, Y. Matsuba, A. Itoh, T. Yokota, D. Hashizume, T. Someya, *Nat. Mater.* **2017**, *16*, 834.
[13] J. Liang, K. Tong, Q. Pei, *Adv. Mater.* **2016**, *28*, 5986.
[14] Mi-S Lee, J. Kim, J. Park, J.-U. Park, *Nanoscale Res. Lett.* **2015**, *10*, 27.
[15] Y. Jiang, S. Ji, J. Sun, J. Huang, Y. Li, G. Zou, T. Salim, C. Wang, W. Li, H. Jin, J. Xu, S. Wang, T. Lei, X. Yan, W. Y. X. Peh, S.-C. Yen, Z. Liu, M. Yu, H. Zhao, Z. Lu, G. Li, H. Gao, Z. Liu, Z. Bao, X. Chen, *Nature* **2023**, *614*, 456.
[16] Z. Liu, X. Wang, D. Qi, C. Xu, J. Yu, Y. Liu, Y. Jiang, Bo Liedberg, X. Chen, *Adv. Mater.* **2017**, *29*, 1603382.
[17] Y. Cao, T G. Morrissey, E. Acome, S I. Allec, B M. Wong, C. Keplinger, C. Wang, *Adv. Mater.* **2017**, *29*, 1605099.
[18] Y. Wang, C. Zhu, R. Pfattner, H. Yan, L. Jin, S. Chen, F. Molina-Lopez, F. Lissel, J. Liu, N I. Rabiah, Z. Chen, J. W. Chung, C. Linder, M F. Toney, B. Murmann, Z. Bao, *Sci. Adv.* **2017**, *3*, e1602076.
[19] S.-Y. Tang, C. Tabor, K. Kalantar-Zadeh, M D. Dickey, *Annu. Rev. Mater. Res.* **2021**, *51*, 381.
[20] T V. Neumann, M D. Dickey, *Adv. Mater. Technol.* **2020**, *5*, 2000070.
[21] Y. Jo, J. H. Hwang, S. S. Lee, Su Y Lee, Y. S. Kim, D.-G. Kim, Y. Choi, S. Jeong, *ACS Appl. Mater. Interfaces* **2022**, *14*, 10747.
[22] Y. G. Park, G. Y. Lee, J. Jang, S. M. Yun, E. Kim, J. U. Park, *Adv. Healthcare Mater.* **2021**, *10*, 2002280.
[23] M. Zadan, C. Chiew, C. Majidi, M. H. Malakooti, *Multifunct. Mater.* **2021**, *4*, 012001.
[24] L. Tang, J. Shang, X. Jiang, *Sci. Adv.* **2021**, *7*, eabe3778.
[25] L. Tang, L. Mou, J. Shang, J. Dou, W. Zhang, X. Jiang, *Mater. Horiz.* **2020**, *7*, 1186.
[26] Li Ding, C. Hang, S. Yang, J. Qi, R. Dong, Y. Zhang, H. Sun, X. Jiang, *Nano Lett.* **2022**, *22*, 4482.
[27] Y. Li, S. Wang, J. Zhang, X. Ma, S. Cao, Y. Sun, S. Feng, T. Fang, D. Kong, *ACS Appl. Mater. Interfaces* **2021**, *14*, 13713.
[28] M. Liao, H. Liao, J. Ye, P. Wan, L. Zhang, *ACS Appl. Mater. Interfaces* **2019**, *11*, 47358.
[29] L.-C. Jia, Y.-F. Jin, J.-W. Ren, L.-H. Zhao, D.-X. Yan, Z.-M. Li, *J. Mater. Chem. C* **2021**, *9*, 2904.
[30] A. Uppal, M. Ralphs, W. Kong, M. Hart, K. Rykaczewski, R. Y. Wang, *ACS Appl. Mater. Interfaces* **2019**, *12*, 2625.
[31] N. Lazarus, B. Hanrahan, *Adv. Mater. Technol.* **2016**, *1*, 1600130.
[32] Y. Wang, Z. Yu, G. Mao, Y. Liu, G. Liu, J. Shang, S. Qu, Q. Chen, R.-W. Li, *Adv. Mater. Technol.* **2019**, *4*, 1800435.
[33] S. Xiang, D. Liu, C. Jiang, W. Zhou, D. Ling, W. Zheng, X. Sun, X. Li, Y. Mao, C. Shan, *Adv. Funct. Mater.* **2021**, *31*, 2100940.

[34] J. Zhang, R. H. Soon, Z. Wei, W. Hu, M. Sitti, *Adv. Sci.* **2022**, *9*, 2203730.
[35] J. Ye, Y.-C. Yao, J.-Y. Gao, S. Chen, P. Zhang, L. Sheng, J. Liu, *Soft Rob.* **2022**, *9*, 1098.
[36] M. Zadan, D K. Patel, A P. Sabelhaus, J. Liao, A. Wertz, L. Yao, C. Majidi, *Adv. Mater.* **2022**, *34*, 2200857.
[37] G. Mao, D. Schiller, D. Danninger, B. Hailegnaw, F. Hartmann, T. Stockinger, M. Drack, N. Arnold, M. Kaltenbrunner, *Nat. Commun.* **2022**, *13*, 4456.
[38] B. Ping, G. Zhou, Z. Zhang, R. Guo, *Front. Bioeng. Biotechnol.* **2023**, *11*, 1118812.
[39] N. Ochirkhuyag, Y. Isano, K. Inoue, H. Ota, *Sens. Diagn.* **2023**, *2*, 290.
[40] M. Kim, H. Lim, S. H. Ko, *Adv. Sci.* **2023**, *10*, 2205795.
[41] X. P. Hao, C. Y. Li, C. W. Zhang, M. Du, Z. Ying, Q. Zheng, Z. L. Wu, *Adv. Funct. Mater.* **2021**, *31*, 2105481.
[42] T. Lu, L. Finkenauer, J. Wissman, C. Majidi, *Adv. Funct. Mater.* **2014**, *24*, 3351.
[43] C. W. Park, Y. G. Moon, H. Seong, S. W. Jung, J.-Y. Oh, B. S. Na, N.-M. Park, S. S. Lee, S. G. Im, J. B. Koo, *ACS Appl. Mater. Interfaces* **2016**, *8*, 15459.
[44] Y.-G. Park, H. Kim, S.-Y. Park, Ju-Y Kim, J.-U. Park, *ACS Appl. Mater. Interfaces* **2019**, *11*, 41497.
[45] R. Abbasi, M. Mayyas, M B. Ghasemian, F. Centurion, J. Yang, M. Saborio, F.-M. Allioux, J. Han, J. Tang, M J. Christoe, K. M. Mohibul Kabir, K. Kalantar-Zadeh, Md. A. Rahim, *J. Mater. Chem. C* **2020**, *8*, 7805.
[46] Y. Lin, O. Gordon, M. R Khan, N. Vasquez, J. Genzer, M D. Dickey, *Lab Chip* **2017**, *17*, 3043.
[47] S. Liang, Y. Li, Y. Chen, J. Yang, T. Zhu, D. Zhu, C. He, Y. Liu, S. Handschuh-Wang, X. Zhou, *J. Mater. Chem. C* **2017**, *5*, 1586.
[48] C. Xiao, J. Feng, H. Xu, R. Xu, T. Zhou, *ACS Appl. Mater. Interfaces* **2022**, *14*, 20000.
[49] M. Tavakoli, M. H. Malakooti, H. Paisana, Y. Ohm, D. G. Marques, P. A. Lopes, A. P. Piedade, A. T. de Almeida, C. Majidi, *Adv. Mater.* **2018**, *30*, 1801852.
[50] J. W. Boley, E L. White, R K. Kramer, *Adv. Mater.* **2015**, *27*, 2355.
[51] P. A. Lopes, D. F. Fernandes, A F. Silva, D. G. Marques, A T. De Almeida, C. Majidi, M. Tavakoli, *ACS Appl. Mater. Interfaces* **2021**, *13*, 14552.
[52] C. Ladd, Ju-H So, J. Muth, M D. Dickey, *Adv. Mater.* **2013**, *25*, 5081.
[53] R. Guo, T. Li, Z. Wu, C. Wan, J. Niu, W. Huo, H. Yu, X. Huang, *ACS Appl. Mater. Interfaces* **2022**, *14*, 37028.
[54] R. Guo, X. Sun, S. Yao, M. Duan, H. Wang, J. Liu, Z. Deng, *Adv. Mater. Technol.* **2019**, *4*, 1900183.
[55] B. Ma, C. Xu, J. Chi, J. Chen, C. Zhao, H. Liu, *Adv. Funct. Mater.* **2019**, *29*, 1901370.
[56] B E. Kelly, I. Bhattacharya, H. Heidari, M. Shusteff, C M. Spadaccini, H K. Taylor, *Science* **2019**, *363*, 1075.
[57] X. Wen, B. Zhang, W. Wang, F. Ye, S. Yue, H. Guo, G. Gao, Y. Zhao, Q. Fang, C. Nguyen, X. Zhang, J. Bao, J T. Robinson, P M. Ajayan, J. Lou, *Nat. Mater.* **2021**, *20*, 1506.
[58] S K. Saha, D. Wang, Vu H. Nguyen, Y. Chang, J S. Oakdale, S.-C. Chen, *Science* **2019**, *366*, 105.
[59] J R. Tumbleston, D. Shirvanyants, N. Ermoshkin, R. Januszieicz, A R. Johnson, D. Kelly, K. Chen, R. Pinschmidt, J P. Rolland, A. Ermoshkin, E T. Samulski, J M. Desimone, *Science* **2015**, *347*, 1349.
[60] M. Hua, D. Wu, S. Wu, Y. Ma, Y. Alsaid, X. He, *ACS Appl. Mater. Interfaces* **2021**, *13*, 12689.
[61] D. Wu, J. Song, Z. Zhai, M. Hua, C. Kim, I. Frenkel, H. Jiang, X. He, *ACS Appl. Mater. Interfaces* **2019**, *11*, 47468.
[62] X. Yang, M. Sun, Y. Bian, X. He, *Adv. Funct. Mater.* **2019**, *29*, 1807615.
[63] Y. Alsaid, S. Wu, D. Wu, Y. Du, L. Shi, R. Khodambashi, R. Rico, M. Hua, Y. Yan, Y. Zhao, D. Aukes, X. He, *Adv. Mater.* **2021**, *33*, 2008235.
[64] S.-Y. Tang, R. Qiao, *Acc. Mater. Res.* **2021**, *2*, 966.
[65] E J. Markvicka, M D. Bartlett, X. Huang, C. Majidi, *Nat. Mater.* **2018**, *17*, 618.
[66] C. J. Thrasher, Z. J. Farrell, N. J. Morris, C. L. Willey, C. E. Tabor, *Adv. Mater.* **2019**, *31*, 1903864.
[67] S. Liu, D S. Shah, R. Kramer-Bottiglio, *Nat. Mater.* **2021**, *20*, 851.
[68] T V. Neumann, E G. Facchine, B. Leonardo, S. Khan, M D. Dickey, *Soft Matter* **2020**, *16*, 6608.
[69] W. Lee, H. Kim, I. Kang, H. Park, J. Jung, H. Lee, H. Park, Ji Su Park, J. M. Yuk, S. Ryu, J.-W. Jeong, J. Kang, *Science* **2022**, *378*, 637.
[70] D. Wu, B. Yao, S. Wu, H. Hingorani, Q. Cui, M. Hua, I. Frenkel, Y. Du, T K. Hsiai, X. He, *Adv. Mater.* **2022**, *34*, 2201772.
[71] W. Zu, Y. Ohm, M. R. Carneiro, M. Vinciguerra, M. Tavakoli, C. Majidi, *Adv. Mater. Technol.* **2022**, *7*, 2200534.
[72] Z. Ma, Q. Huang, Qi Xu, Q. Zhuang, X. Zhao, Y. Yang, H. Qiu, Z. Yang, C. Wang, Y. Chai, Z. Zheng, *Nat. Mater.* **2021**, *20*, 859.
[73] S. Zhu, Ju-H So, R. Mays, S. Desai, W R. Barnes, B. Pourdeyhimi, M D. Dickey, *Adv. Funct. Mater.* **2013**, *23*, 2308.
[74] K. Parida, G. Thangavel, G. Cai, X. Zhou, S. Park, J. Xiong, P. S. Lee, *Nat. Commun.* **2019**, *10*, 2158.
[75] H. Li, R. Qiao, T P. Davis, S.-Y. Tang, *Biosensors* **2020**, *10*, 196.
[76] Z J. Farrell, C J. Thrasher, A E. Flynn, C E. Tabor, *ACS Appl. Nano Mater.* **2020**, *3*, 6297.
[77] X. Li, M. Li, J. Xu, J. You, Z. Yang, C. Li, *Nat. Commun.* **2019**, *10*, 3514.
[78] M. R. Khan, C. Trlica, J.-H. So, M. Valeri, M. D. Dickey, *ACS Appl. Mater. Interfaces* **2014**, *6*, 22467.
[79] E. Andrzejewska, in *Three-Dimensional Microfabrication Using Two-Photon Polymerization: Fundamentals, Technology, and Applications*, Elsevier Inc., New York **2016**, pp. 62–81.
[80] T. T. H. Luu, Z. Jia, A. Kanaev, L. Museur, *J. Phys. Chem. B* **2020**, *124*, 6857.
[81] N. Désilles, C. Gautrelet, L. Lecamp, P. Lebaudy, C. Bunel, *Eur. Polym. J.* **2005**, *41*, 1296.
[82] J. E. Park, H. S. Kang, M. Koo, C. Park, *Adv. Mater.* **2020**, *32*, 2070277.
[83] Y. H. Cho, Y.-G. Park, S. Kim, J.-U. Park, *Adv. Mater.* **2021**, *33*, 2005805.
[84] Y.-G. Park, I. Yun, W Gi Chung, W. Park, D Ha Lee, J.-U. Park, *Adv. Sci.* **2022**, *9*, 2104623.
[85] S. A. Rahman, S. A. Khan, M. M. Rehman, W.-Y. Kim, *Nanomaterials* **2022**, *12*, 1026.
[86] M. Hua, S. Wu, Y. Ma, Y. Zhao, Z. Chen, I. Frenkel, J. Strzalka, H. Zhou, X. Zhu, X. He, *Nature* **2021**, *590*, 594.
[87] S. Wu, M. Hua, Y. Alsaid, Y. Du, Y. Ma, Y. Zhao, C.-Y. Lo, C. Wang, D. Wu, B. Yao, J. Strzalka, H. Zhou, X. Zhu, X. He, *Adv. Mater.* **2021**, *33*, 2007829.
[88] D. Sun, J. Zhang, H. Li, Z. Shi, Qi Meng, S. Liu, J. Chen, X. Liu, *Polymers* **2021**, *13*, 1889.
[89] Y. Yan, Y. Zhao, Y. Alsaid, B. Yao, Y. Zhang, S. Wu, X. He, *Adv. Intell. Syst.* **2021**, *3*, 2000234.
[90] P. Shi, Y. Zhao, Z. Liu, X. He, *J. Compos. Mater.* **2022**, *57*, 633.
[91] Y. Zhao, Q. Li, Z. Liu, Y. Alsaid, P. Shi, M. Khalid Jawed, X. He, *Sci Robot* **2023**, *8*, eadf4753.